



## Rail potential control with train diagram optimization in multitrain DC traction power system

Chengqian Zhu, Guifu Du, Yawen Ding, Weiguo Huang, Jun Wang, Mingdi Fan & Zhongkui Zhu

To cite this article: Chengqian Zhu, Guifu Du, Yawen Ding, Weiguo Huang, Jun Wang, Mingdi Fan & Zhongkui Zhu (2021): Rail potential control with train diagram optimization in multitrain DC traction power system, International Journal of Rail Transportation, DOI: [10.1080/23248378.2021.1964391](https://doi.org/10.1080/23248378.2021.1964391)

To link to this article: <https://doi.org/10.1080/23248378.2021.1964391>



Published online: 17 Aug 2021.



Submit your article to this journal



Article views: 3



View related articles



View Crossmark data



# Rail potential control with train diagram optimization in multitrain DC traction power system

Chengqian Zhu, Guifu Du, Yawen Ding, Weiguo Huang, Jun Wang, Mingdi Fan and Zhongkui Zhu

School of Rail Transportation, Soochow University, Suzhou, China

## ABSTRACT

Currently, abnormally elevated rail potential exists in the DC traction power system, which greatly threatens the safe operation of the line. In order to realize the reflux safety, timetable optimization of multitrain based on improved Seeker Optimization Algorithm (SOA) is proposed to suppress the rail potential of the system. Firstly, the simulation model of the system is built and the calculation process of rail potential is proposed. Secondly, an optimization model based on maximum rail potential is formulated, where the dwell time is the decision variable and is adjusted to change the regenerative power distribution of the system. Finally, the improved SOA is used to handle the optimization model. Compared with the maximum rail potential before optimization, the simulation results demonstrate that the maximum rail potential is reduced by 55.5% with the proposed method, which greatly improves the reflux safety of the multi-train subway system.

## ARTICLE HISTORY

Received 10 April 2021  
Revised 1 August 2021  
Accepted 2 August 2021

## KEYWORDS

DC traction power system;  
rail potential; power  
distribution; seeker  
optimization algorithm

## 1. Introduction

At present, DC traction power system widely uses the running rails as the backflow conductor in the system [1,2]. Because of the resistance of the rails, there is a certain potential between the rails and earth, which is called rail potential [3]. Part of the current in the rails will flow to the earth, forming stray current [4]. Excessive rail potential and stray current will endanger the safety of passengers and the equipment [5,6]. Under normal operation conditions, the rail potential should be controlled within 90 V [7]. Over Voltage Protection Devices (OVPDs) are usually installed at each traction substation (TSS). If the rail potential on the OVPD exceeds the safety limit of 90 V, OVPD will be triggered to connect the rails to earth, so as to control the rail potential [8].

During the dynamic operation of Guangzhou subway line, the rail potential is generally high, resulting in frequent action of the OVPDs at 2 or 3 stations in the line. In order to reduce the impact of the elevated rail potential on the operation safety of the subway and the personal safety of passengers, OVPDs are temporarily closed manually at these stations. However, this will cause different degrees of electrical corrosion to the tunnel, the structural steel of the track bed and the nearby metal pipeline. Besides, the line detection results indicate that the parameters of the reflux system are normal, but the rail potential still exceeds the standard limit. The subsequent studies demonstrate that the abnormally elevated rail potential is related to the power distribution of the system.

Regarding the suppression methods of rail potential, relevant studies have been carried out. Alamuti et al. proposed a reverse diode grounding method to limit the reflux safety parameters [9].

Xu et al. studied the influence of train operation conditions on the reflux safety parameters [8]. The research shows that when the train is in the accelerating or braking condition, the rail potential will be higher and the rail potential at the train is the highest in the whole line. Tzeng et al. studied the influence of the impedance connector between multiple lines in the Taipei MRT on the reflux safety parameters. Through simulations and field tests, it is proved that removing the impedance connector between multiple lines can effectively reduce the rail potential [4,10]. In order to protect personal safety, when the rail potential in the line is high, OVPD will be triggered to connect the running rails to the ground. If OVPD works frequently, massive stray current will leak to the ground, causing electrochemical corrosion, which seriously affects the safe operation of the system. It proves that OVPD cannot fundamentally handle the excessive rail potential.

A desirable timetable is extremely significant for the high-quality operation of the multi-train subway system. Many scholars have studied the timetable optimization for the efficient operation of the system. Yang et al. [11] proposed a cooperative scheduling scheme to optimize the timetable to maximize the overlapping time between the braking train and the accelerating train. Su et al. [12] studied the integrated timetable and the speed profiles. Pena et al. [13] designed the timetable for maximum utilization of regenerative energy. Chen et al. [14] adopted Dijkstra algorithm to optimize the timetable, which has been evaluated on Shenzhen metro network. The test results showed that the optimized last train timetable greatly improves the accessibility of the subway network and enhances the transfer connections between the last trains. Zhu et al. [15] employed genetic algorithm to solve a bi-level model to design the timetable for Beijing Yizhuang subway line. After the evaluation of real cases, the timetable obtained by the method can reduce the time cost of passengers. Although the research above can guarantee the energy saving of the system and the convenience of passengers, they ignore the safe operation of the system.

Recently, considering the variable output characteristics of fuel cells, Li proposed an online extremum seeking method based on the adaptive recursive least square algorithm to achieve the optimal power distribution between proton exchange membrane fuel cell and supercapacitor [16]. Li also proposed a hierarchical performance enhancement control strategy to search the optimal trajectory under the condition of multi-objective constraints and nonlinear system, respectively [17]. The maximum rail potential in the whole line is optimized by adjusting the timetable to change the regenerative power distribution of the system in this paper. It is also a complex non-linear optimization problem to control the rail potential by adjusting the dwell time of each train under the complex working conditions of the system.

In this paper, an improved Seeker Optimization Algorithm (SOA) is employed to handle the optimization model. SOA simulates the intelligent search behaviour of human beings, it finds the optimal solution in the continuous search space relying on its own experiences, memory and uncertainties consideration [18–20]. In addition, this paper adds a chaotic optimization method to SOA algorithm to prevent the SOA algorithm from easily falling into a local optimum and causing the algorithm to stagnate [21]. The improved SOA is proposed to adjust the trains' dwell time within reasonable range, so that the power distribution is greatly adjusted and the rail potential is effectively controlled. With the rapid development of automatic train operation, the optimization of train diagram will be put on the agenda. Real-time optimization of train diagram is essential to guarantee the safety and economy of the subway system.

## 2. System description

Due to the electrical connectivity of the catenaries and rails, the rail potential of the entire line is greatly affected by the power transferring over zones [22,23]. Under the complex working conditions of the system, the train absorbs energy from the catenary under traction condition and returns energy to the catenary under braking condition. For the long transmission distance of traction current, the network loss  $P_{loss}$  exists in the line. When the regenerative energy is absorbed by the train running at the far end, the rail potential of the line will rise greatly [24].

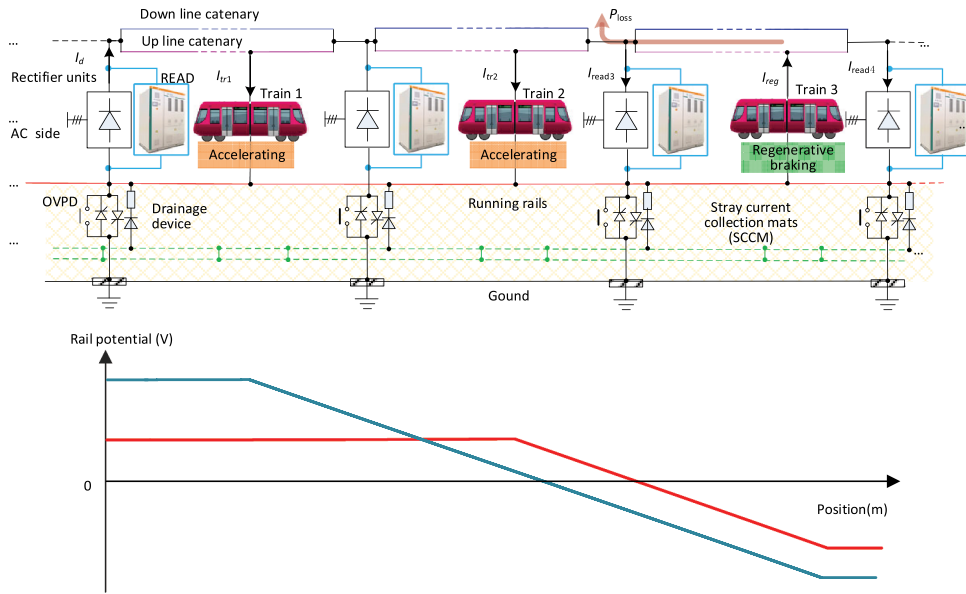


**Figure 1.** Diagram of DC traction power system.

As shown in Figure 1, when the Train 1 in the first interval is under the bilateral power supply model, the current absorbed by accelerating train  $I_{tr}$  consists of the traction current provided by TSS  $I_d$  and the regenerative braking power transferring over zones. The total regenerative braking current  $I_{reg}$  is absorbed by the accelerating trains and the adjacent regenerative braking energy absorbing devices (READs)  $I_{read}$ , which will be activated to consume the residual energy when catenary voltage exceeds the limit. The rail potential at the position of the accelerating trains in the first two intervals is also shown in Figure 1. When the regenerative braking train in the interval 3 supply power for the accelerating train in the interval 2, the transmission distance is shorter and the rail potential is relatively lower compared with the regenerative braking train in the interval 3 supply power for the accelerating train in interval 1.

### 3. Formulation of the model

#### 3.1. Simulation model

Figure 2 shows the model of DC traction power system. The train is regarded as a variable power source, such as  $P_2$  or  $P_4$  in the model. The TSS mainly consists of 24 pulse uncontrolled rectifier units and READ.  $y_{CN}$  is the internal resistance of the rectifier units,  $P_N$  is the output power of the rectifier units and the output characteristics of which is shown as line I. When the catenary voltage is between the range of no-load voltage  $U_0$  and working voltage  $U_{max}$ , TSS is out of operation and the external characteristic curve is depicted as II. As depicted in curve III, the READ will consume the extra regenerative braking energy when the catenary voltage increases abnormally and maintains the voltage constantly at  $U_{max}$ . In the traction network,  $U_{un}$  and  $U_{dn}$  are voltage of the up line and down line at node  $n$  respectively;  $z_{un}$  and  $z_{dn}$  are the impedance of up line and down line between  $x_n$  and  $x_{(n+1)}$ , respectively;  $U_{rn}$  and  $U_{sn}$  are the potential of running rails and stray current collection mats (SCCM) at node  $n$  respectively;  $z_{rn}$  and  $z_{sn}$  are the impedance of rails and SCCM between  $x_n$  and  $x_{(n+1)}$ , respectively.

Based on the mixed parameter model of the reflux system in Figure 2, the differential equations for rail potential  $u_r(x)$ , the potential of SCCM  $u_s(x)$ , the current of rail  $i_r(x)$  and SCCM  $i_s(x)$  can be established as Equation (1):

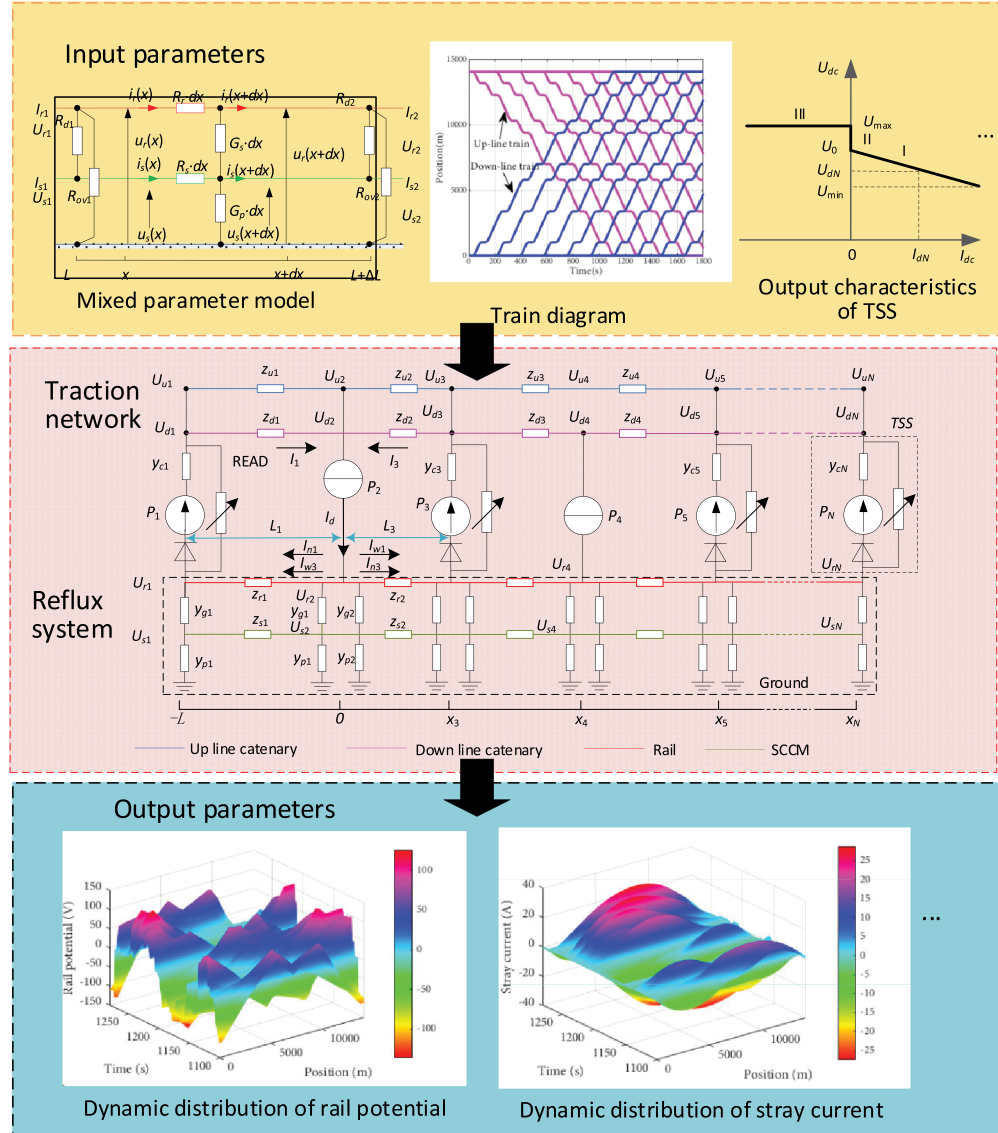


Figure 2. The simulation model of DC traction power system.

$$\begin{bmatrix} \dot{u}_r(x) \\ \dot{u}_s(x) \\ \dot{i}_r(x) \\ \dot{i}_s(x) \end{bmatrix} = \begin{bmatrix} 0 & 0 & -R_r & 0 \\ 0 & 0 & 0 & -R_s \\ -G_s & G_s & 0 & 0 \\ G_s & -(G_p + G_s) & 0 & 0 \end{bmatrix} \begin{bmatrix} u_r(x) \\ u_s(x) \\ i_r(x) \\ i_s(x) \end{bmatrix} \quad (1)$$

The solution of Equation (1) is shown as Equation (2):

$$\begin{cases} u_r(x) = C_1 e^{-\alpha x} + C_2 e^{\alpha x} + C_3 e^{-\beta x} + C_4 e^{\beta x} \\ u_s(x) = \frac{\alpha}{R_r} (C_1 e^{-\alpha x} - C_2 e^{\alpha x}) + \frac{\beta}{R_r} (C_3 e^{-\beta x} - C_4 e^{\beta x}) \\ i_r(x) = (1 - \frac{\alpha^2}{G_s R_r}) (C_1 e^{-\alpha x} + C_2 e^{\alpha x}) + (1 - \frac{\beta^2}{G_s R_r}) (C_3 e^{-\beta x} + C_4 e^{\beta x}) \\ i_s(x) = r_\alpha (C_1 e^{-\alpha x} - C_2 e^{\alpha x}) + r_\beta (C_3 e^{-\beta x} - C_4 e^{\beta x}) \end{cases} \quad (2)$$

where  $R_r$  and  $R_s$  are the resistances of the running rails and SCCM.  $G_s$  and  $G_p$  are the transition conductances of rails to SCCM and SCCM to earth respectively.  $\alpha = \sqrt{\frac{m+n}{2} + \sqrt{\frac{(m-n)^2}{4} + mk}}$ ,  $\beta = \sqrt{\frac{m+n}{2} - \sqrt{\frac{(m-n)^2}{4} + mk}}$ ,  $m = R_r G_s$ ,  $n = R_s (G_s + G_p)$ ,  $k = R_s G_s$ , the indeterminate coefficients  $C_1 \sim C_4$  can be obtained by the boundary conditions of the interval. Then, the equivalent resistances of rails and SCCM  $z_{r1}, z_{s1}$ , and the equivalent conductances of rails to SCCM and SCCM to earth  $y_{g1}, y_{p1}$  can be obtained as depicted in the lumped parameter model of the reflux system in Figure 2.

### 3.2. Calculation method of rail potential with multiple trains and multiple TSSs operating

After the model equivalence and parameter correction are carried out, the power flow calculation of the system will be performed. Based on the simulation model shown in Figure 2, the voltage  $U = [U_1, U_2, \dots, U_N]$ , the current  $I = [I_1, I_2, \dots, I_N]$  and the positions  $X = [x_1, x_2, \dots, x_N]$  in the whole line at any time can be obtained. Then, the influence of load current distribution on rail potential is analysed as follows:

When  $P_2$  in the first power supply interval is under unilateral side power supply mode and the second TSS is out of operation. For simplicity of calculation, the train node is regarded as the origin. The differential equations of rail potential  $u(x)$  and the current of running rail  $i(x)$  under this condition are established as Equation (3):

$$\begin{cases} du(x) = -i(x) \cdot Rr \cdot dx \\ di(x) = -u(x)/(Rg/dx). \end{cases} \quad (3)$$

The general solution of  $i(x)$  under unilateral side power supply mode is shown as Equation (4):

$$i(x) = C_1 \cdot e^{\gamma \cdot x} + C_2 \cdot e^{-\gamma \cdot x} \quad (4)$$

where  $R_r$  represents the resistance of rails,  $R_g$  represents the transition resistance of rails to ground,  $\gamma = \sqrt{\frac{R_r}{R_g}}$ ,  $C_1$  and  $C_2$  are indeterminate coefficients.

When the internal load current of the power supply arm  $I_n$  is taken into account, the boundary conditions under unilateral side power supply mode are  $i(0) = I_n$ ,  $i(-L) = I_n$ , then, the load current can be expressed as Equation (5):

$$i_n(x) = \frac{I_n}{sh(\gamma \cdot L)} \cdot \{sh[\gamma \cdot (L+x)] - sh(\gamma \cdot x)\}. \quad (5)$$

When the external load current of the power supply arm  $I_w$  is taken into account, the boundary conditions under unilateral side power supply mode are  $i(0) = I_w$ ,  $i(\infty) = 0$ , then, the load current can be expressed as Equation (6):

$$i_w(x) = I_w \cdot e^{-\gamma \cdot x}. \quad (6)$$

According to Equation (5) and (6), the stray current  $i_{yn}(x)$  and  $i_{yw}(x)$  caused by internal and external load current of power supply arm can be expressed as the difference between load current and the current of the rails:

$$\begin{cases} i_{yn}(x) = I_n - i_n(x) = I_n \cdot \{1 - \frac{sh[\gamma \cdot (L+x)] - sh(\gamma \cdot x)}{sh(\gamma \cdot L)}\} \\ i_{yw}(x) = I_w - i_w(x) = I_w \cdot (1 - e^{-\gamma \cdot x}). \end{cases} \quad (7)$$

The variation of the rail current is called the intensity of stray current which is the derivative of  $i(x)$ . The intensity of stray current  $i_{mn}(x)$  and  $i_{mw}(x)$  caused by the internal and external current of power supply arm can be expressed as Equation (8):

$$\begin{cases} i_{mn}(x) = \frac{di_n(x)}{dx} = \frac{\gamma \cdot I_n}{sh(\gamma \cdot L)} \cdot \{ch[\gamma \cdot (L + x)] - ch(\gamma \cdot x)\} \\ i_{mw}(x) = \frac{di_w(x)}{dx} = \gamma \cdot I_w \cdot e^{-\gamma \cdot x}. \end{cases} \quad (8)$$

The rail potential caused by internal and external load current of power supply arm  $u_n(x)$  and  $u_w(x)$  can be obtained by product of the intensity of stray current and  $R_g$  respectively:

$$\begin{cases} u_n(x) = i_{mn}(x) \cdot R_g = \frac{Z_{cr} \cdot I_n}{sh(\gamma \cdot L)} \cdot \{ch[\gamma \cdot (L + x)] - ch(\gamma \cdot x)\} \\ u_w(x) = i_{mw}(x) \cdot R_g = R_g \cdot \gamma \cdot I_w \cdot e^{-\gamma \cdot x} = Z_{cr} \cdot I_w \cdot e^{-\gamma \cdot x} \end{cases} \quad (9)$$

where  $Z_{cr} = \sqrt{R_r \cdot R_g}$ .

The stray current intensity is closely related to the load current, and is related to the calculation of rail potential. The distribution relationship between the internal and external load current of the power supply arm is analysed as follows:

The internal and external rail potential of the power supply arm at the position of  $P_2$  are the same, which satisfies Equation (10):

$$u_n(0^+) = u_w(0^-). \quad (10)$$

Based on Equation (9) and (10), the distribution relationship between the internal and external load current of the power supply arm can be obtained as Equation (11):

$$\frac{I_w}{I_n} = \frac{ch(\gamma \cdot L) - 1}{sh(\gamma \cdot L)} = \frac{e^{\gamma \cdot L} - 1}{e^{\gamma \cdot L} + 1} = D. \quad (11)$$

Under the unilateral side power supply mode, the total load current  $I_d$  is the sum of  $I_n$  and  $I_w$ , that is,  $I_d = I_n + I_w$ . Then, the relationship between  $I_n$ ,  $I_w$  and  $I_d$  can be obtained as Equation (12):

$$\begin{cases} I_n = \frac{1}{1+D} \cdot I_d = \frac{1+e^{-\gamma \cdot L}}{2} \cdot I_d \\ I_w = \frac{D}{1+D} \cdot I_d = \frac{1-e^{-\gamma \cdot L}}{2} \cdot I_d \end{cases} \quad (12)$$

where  $D$  is the proportional coefficient of the internal and external load current of the power supply arm.

By substituting Equation (12) into Equation (9), the relationship between the total load current  $I_d$  and the rail potential  $u(x)$  is obtained.

In the multi-train DC traction power system, bilateral power supply mode is the most common power supply mode. Based on the research on the unilateral side power supply of current distribution, the extended analysis of the bilateral power supply mode is carried out. The analysis idea is approximately considered as the superposition of two unilateral side power supply modes.

As depicted in Figure 2, in the first bilateral supply interval, the load current  $I_d$  is provided by the TSSs at the first and third cross section. Assuming that the terminal voltages of the two TSSs are the same, the load current  $I_1$  and  $I_3$  provided by the two TSSs are inversely proportional to the supply distance, which are expressed as Equation (13)

$$\begin{cases} I_1 = I_d \cdot \frac{L_3}{L_1 + L_3} \\ I_3 = I_d \cdot \frac{L_1}{L_1 + L_3} \end{cases} \quad (13)$$

Based on Equation (12) and (13), the internal and external load current of the TSSs at the first and third cross section is shown as Equation (14) and (15) respectively:

$$\begin{cases} I_{n1} = \frac{1}{1+D_1} \cdot I_d \cdot \frac{L_3}{L_1 + L_3} \\ I_{w1} = \frac{D_1}{1+D_1} \cdot I_d \cdot \frac{L_3}{L_1 + L_3} \\ D_1 = \frac{e^{\gamma \cdot L_1} - 1}{e^{\gamma \cdot L_1} + 1}. \end{cases} \quad (14)$$

$$\begin{cases} I_{n3} = \frac{1}{1+D_3} \cdot I_d \cdot \frac{L_1}{L_1+L_3} \\ I_{w3} = \frac{D_3}{1+D_3} \cdot I_d \cdot \frac{L_1}{L_1+L_3} \\ D_3 = \frac{e^{\gamma \cdot L_3} - 1}{e^{\gamma \cdot L_3} + 1}. \end{cases} \quad (15)$$

In the power supply arm  $L_1$ ,  $i(x)$ ,  $i_y(x)$ ,  $i_m(x)$  and  $u(x)$  can be calculated by superimposing each component caused by the distribution of load current:

$$i(x) = i_{n1} + i_{w3} = \frac{I_{n1}}{sh(\gamma \cdot L_1)} \cdot \{sh[\gamma \cdot (L_1 + x)] - sh(\gamma \cdot x)\} + I_{w3} \cdot e^{\gamma \cdot x} \quad (16)$$

$$i_y(x) = i_{yn1} + i_{yw3} = I_{n1} \cdot \left\{ 1 - \frac{sh[\gamma \cdot (L_1 + x)] - sh(\gamma \cdot x)}{sh(\gamma \cdot L_1)} \right\} + I_{w3} \cdot (1 - e^{\gamma \cdot x}) \quad (17)$$

$$i_m(x) = i_{mn1}(x) + i_{mw3}(x) = \frac{\gamma \cdot I_{n1}}{sh(\gamma \cdot L_1)} \cdot \{ch[\gamma \cdot (L_1 + x)] - ch(\gamma \cdot x)\} + \gamma \cdot I_{w3} \cdot e^{\gamma \cdot x} \quad (18)$$

$$u(x) = u_{n1} + u_{w3} = \frac{R_g \cdot \gamma \cdot I_{n1}}{sh(\gamma \cdot L_1)} \cdot \{ch[\gamma \cdot (L_1 + x)] - ch(\gamma \cdot x)\} + R_g \cdot \gamma \cdot I_{w3} \cdot e^{\gamma \cdot x}. \quad (19)$$

The distribution of load current that causes stray current can be calculated in each power supply interval. The total rail potential in each interval is obtained by superimposing each component of rail potential caused by corresponding load current.

In order to facilitate the analysis of rail potential, the coordinates of an arbitrary load node  $m$  is taken as the origin coordinate, and the coordinates of other source nodes are adopted the relative coordinates. For another source node  $n$  ( $n \neq m$ ), the relative coordinates of  $m$  is  $(x_n - x_m)$ . Then, the general solution of Equation (3) is shown as Equation (20):

$$\begin{cases} u(x) = C_{nm1} \cosh(\gamma \cdot x) + C_{nm2} \sinh(\gamma \cdot x) \\ i(x) = -\left(\frac{1}{\sqrt{R_r \cdot R_g}}\right)(C_{nm1} \sinh(\gamma \cdot x) + C_{nm2} \cosh(\gamma \cdot x)). \end{cases} \quad (20)$$

Assuming that the ratio of the current provided by source node  $n$  to load node  $m$  is  $\mu_{nm}$ , the boundary conditions are:  $i(0) = \mu_{nm} I_d$  and  $i(x_n - x_m) = \mu_{nm} I_d$ , the indeterminate coefficients  $C_{mn1}$  and  $C_{nm2}$  can be obtained:

$$\begin{cases} C_{nm1} = \frac{\mu_{nm} I_d \sqrt{R_r \cdot R_g} (\cosh(\gamma \cdot (x_n - x_m)) - 1)}{\sinh(\gamma \cdot (x_n - x_m))} \\ C_{nm2} = -\mu_{nm} I_d \sqrt{R_r \cdot R_g}. \end{cases} \quad (21)$$

The component of rail potential at load node  $m$  can be expressed as follows:

$$u_{nm}(0) = C_{nm1} = \frac{\mu_{nm} I_d \sqrt{R_r \cdot R_g} (\cosh(\gamma \cdot (x_n - x_m)) - 1)}{\sinh(\gamma \cdot (x_n - x_m))}. \quad (22)$$

The total rail potential  $u_{total}$  at load node  $m$  is the superposition of all the components of rail potential formed by other source nodes supplying power to node  $m$ :

$$u_{total}(0) = I_d \sqrt{R_r \cdot R_g} \cdot \sum_{n=1,n}^N [\mu_{mn} \cdot \left( \frac{\cosh(\gamma \cdot (x_n - x_m)) - 1}{\sinh(\gamma \cdot (x_n - x_m))} \right)]. \quad (23)$$

### 3.3. Establishment of optimization model based on maximum rail potential

In this paper, the regulation of the train diagram is used to manage the regenerative braking power of the system, so as to realize the suppression of the rail potential of the line. However, just optimizing the rail potential by adjusting the train diagram may cause huge total energy consumption of the system. At present, many regenerative braking energy utilization strategies, such as energy storage devices and regenerative braking energy feedback devices, have been widely adopted in DC traction power system. The application of these devices can effectively achieve energy conservation. While the reflux safety issue of the system has not been completely addressed. At the same time, the reflux safety parameters are greatly affected by the train diagram, which can be suppressed through proper timetable adjustment. The rail potential is a function of dwell time and the range of which is set to  $a \sim b$ . Assuming that the trains' dwell time of up line and down line is  $\mathbf{X} = [t_{u1}, t_{u2}, \dots, t_{un}, t_{d1}, t_{d2}, \dots, t_{dn}]$ . According to the above simulation model, when the dwell time of each train is determined, the rail potential  $U_r$  of each node can be calculated according to Equation (23), the optimization model is shown as Equation (24):

$$\begin{aligned} \min \quad & f(\mathbf{X}) = \max(|U_{rn}|) \\ \text{s. t. } & \mathbf{X} = [t_{u1}, t_{u2}, \dots, t_{un}, t_{d1}, t_{d2}, \dots, t_{dn}] \\ & a \leq t_{ui} \leq b, i=1, 2, \dots, n \\ & a \leq t_{di} \leq b, i=1, 2, \dots, n \\ & T_u, T_d \leq T_{\max} \end{aligned} \quad (24)$$

where  $t_{un}$  and  $t_{dn}$  are the dwell time of up line and down line of the  $n$ -th train, which are all rounded.  $T_u$  and  $T_d$  represent the total travel time of up line train and down line train, respectively.  $T_{\max}$  is the maximum total travel time.

## 4. Optimization method based on improved seeker optimization algorithm

Seeker Optimization Algorithm (SOA) directly simulates the intelligent search behaviour of human beings and applies their intelligent behaviour to search for the solutions. Human's random search behaviour can be understood as follows: there may be better solutions around the good solution in the continuous search space, and the optimal solution may exist in the field of the better solution. Therefore, when the seeker is in a good position, a smaller area will be searched; when the searcher is in a bad position, a larger area will be searched. The directions and step length are obtained through individual and social cognition.

Supposing that there is a population of  $m$  individuals in  $j$ -D search space, the  $i$ -th individual is a  $j$ -D vector  $\vec{\mathbf{x}}_i = (x_{i1}, x_{i2}, \dots, x_{ij})$ ,  $i = 1, 2, \dots, m$ . Each individual is a potential solution whose function value is obtained by substituting the vector  $\vec{\mathbf{x}}_i$  into the objective function  $f(\mathbf{X})$ .

### 4.1. Search direction

#### 4.1.1. Egoistic behaviour

Human intelligence comes from social communication, and human society is an intelligent community. As an individual is in the intelligent community, each individual has its own selfish behaviour, relying on its own experience and moving towards the best position in its history through cognitive learning. The  $i$ -th individual's egoistic direction is expressed as Equation (25):

$$\vec{d}_{ij,ego}(t) = sign(\vec{g}_{i,best} - \vec{x}_i(t)) \quad (25)$$

where  $\vec{g}_{i,best}$  is the best position of  $i$ -th individual so far;  $t$  represents the current iteration number;  $sign(\cdot)$  is the symbolic function.

#### 4.1.2. Altruistic behaviour

Altruistic behaviour follows the principle of group priority. Each individual cooperates with each other, communicates information, shares social experiences within the population, and constantly adjusts their behaviour to achieve a common purpose. Each individual learns through society to approach the optimal solution. The altruistic behaviour of the  $i$ -th individual can be expressed as Equation (26):

$$\vec{d}_{ij,alt}(t) = \text{sign}(\vec{p}_{i,best} - \vec{x}_i(t)) \quad (26)$$

where  $\vec{p}_{i,best}$  is the best position of the group so far.

#### 4.1.3. Proactive behaviour

Proactive behaviour is the goal-oriented behaviour shown by intelligent individuals, which can predict and guide the future behaviours by the past behaviours and the results. Therefore, the  $i$ -th individual adaptively takes active measures according to its past behaviour and the feedback of the environment, and presents the goal-oriented proactive behaviour as shown in Equation (27):

$$\vec{d}_{ij,pro}(t) = \begin{cases} -\vec{D}_{ij}f(\vec{g}_{i,best}) \geq f(\vec{x}_i) \\ \vec{D}_{ij}f(\vec{g}_{i,best}) < f(\vec{x}_i) \end{cases} \quad (27)$$

where  $f(\vec{g}_{i,best})$  is the function value of  $\vec{g}_{i,best}$ ,  $\vec{D}_{ij}$  is the final search direction which is shown as Equation (28) and each of its element is set to 1 in the first iteration.

The final search direction is calculated by the 3 directions above, which is shown in Equation (28):

$$\vec{D}_{ij} = \text{sign}(\omega \vec{d}_{ij,pro} + r_1 \vec{d}_{ij,ego} + r_2 \vec{d}_{ij,alt}) \quad (28)$$

where  $\omega = \frac{(\tau_{\max} - \tau)}{\tau_{\max}}$ ,  $\tau$  and  $\tau_{\max}$  are the current iteration times and the maximum iteration times;  $r_1$  and  $r_2$  are the random numbers in the interval  $[0, 1]$ .

### 4.2. Search step

According to the intermediary value theorem, in a continuous search space, the function value of a point in an area near the extreme point is proportional to its distance from the extreme point. Therefore, when the individual's position is better, there may be an optimal solution nearby. At this time, the individual will search within a smaller range; and when the individual's position is poor, the individual will expand the search range.

A fuzzy system is based on the need for humans to use natural language to describe complex systems. The ambiguity of human thinking shows that fuzzy logic plays an important role in describing human thinking. The uncertain reasoning behaviour of SOA is to use the approximation ability of the fuzzy system to simulate the intelligent search behaviour of human, thereby establishing the connection between perception (function value) and behaviour (step length). In this paper, the Gaussian membership function is used to represent the fuzzy variable of search step, as shown in Equation (29):

$$u(\alpha) = e^{\frac{-\alpha^2}{2\delta^2}} \quad (29)$$

Figure 3 depicts the Gaussian membership function,  $\delta$  is the membership parameter and  $u(3\delta) = 0.0111$ . The minimum membership value is set to  $u_{\min} = 0.0111$ , therefore, the input variable range is  $[-3\delta, 3\delta]$ .

The fuzzy system of the optimization problem described in language is as follows: at the  $t$ -th iteration,  $m$  function values  $f(x_1(t)), \dots, f(x_i(t)), \dots, f(x_m(t))$  are arranged in descending order, and

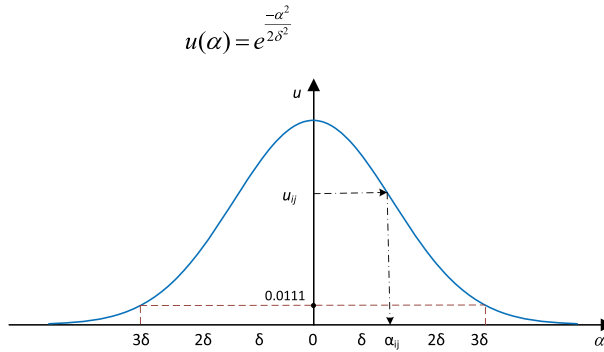


**Figure 3.** Gaussian membership function.

their orders as the inputs of fuzzy reasoning are  $1, 2, \dots, m$  after sorting. In the process of fuzzification, the linear membership function expression (30) is established and the membership value  $u_i$  is proportional to the order of the function value:

$$u_i = u_{\max} - \frac{(m - i) \cdot (u_{\max} - u_{\min})}{m - 1} \quad (30)$$

where  $i$  represents the order of the current individual after sorting. In this paper,  $u_{\max} = 0.95$  and  $u_{\min} = 0.0111$ .

In addition to the defined membership values of the best position and the worst position, in other positions, the corresponding membership value of the  $i$ -th function value in the  $j$ -D search space is determined by Equation (31), the randomness of human search behaviour is simulated in this way:

$$u_{ij} = \text{rand}(u_i, 1) \quad (31)$$

where  $\text{rand}(u_i, 1)$  means the uniformly distribution on  $[u_i, 1]$ .

As shown in Figure 3, the step length of the  $i$ -th individual in  $j$ -D search space can be obtained based on the defuzzification process (32):

$$\alpha_{ij} = \delta_{ij} \sqrt{-\ln(u_{ij})} \quad (32)$$

where  $\overrightarrow{\delta_{ij}} = \omega \cdot |\vec{x}_{\min} - \vec{x}_{\max}|$  and  $\vec{x}_{\min}$ ,  $\vec{x}_{\max}$  are the best and worst positions of current iteration, respectively.

Finally, based on Equation (28) and Equation (32), the  $i$ -th individual updates its position according to Equation (33):

$$x_{ij}(t + 1) = x_{ij}(t) + \alpha_{ij}(t) \cdot \overrightarrow{D}_{ij}(t) \quad (33)$$

#### 4.3. Chaos optimization

In order to prevent the local aggregation of individuals, this paper introduces a chaotic optimization method. The ergodic characteristics of chaotic variables can traverse all states in a local range without repetition, avoiding the algorithm from falling into local extreme points.

Logistic equation is a typical chaotic system, which is expressed as Equation (34):

$$y_{n+1} = \mu y_n (1 - y_n), \mu \in [0, 4], y_n \in [0, 1] \quad (34)$$

where  $\mu$  is the Logistic parameter,  $y_n$  is the output of the system and  $n$  is the number of iterations. The closer  $\mu$  is to 4, the closer  $y$  is to uniform distribution in [0, 1].

In this paper, the  $\vec{g}_{i,best}$  is normalized by Equation (35):

$$y_i = \frac{(\vec{g}_{i,best} - \vec{R}_{\min})}{\vec{R}_{\max} - \vec{R}_{\min}} \quad (35)$$

where  $y_i$  is the normalized result of  $\vec{g}_{i,best}$ ,  $\vec{R}_{\min}$  and  $\vec{R}_{\max}$  are the upper and lower bounds of each individual, respectively.

After normalization, the individual chaotic sequence  $y_i^*$  is obtained based on Equation (34). Then,  $y_i^*$  is mapped back to the original space by Equation (36):

$$\vec{g}_{i,best}^* = \vec{R}_{\max} + (\vec{R}_{\max} - \vec{R}_{\min}) \cdot y_i^* \quad (36)$$

where  $\vec{g}_{i,best}^*$  is chaotic adaptation value which is obtained after chaos mapping. If  $f(\vec{g}_{i,best}^*) < f(\vec{g}_{i,best})$ , then  $\vec{g}_{i,best} = \vec{g}_{i,best}^*$ , else  $\vec{g}_{i,best}$  remains unchanged.

The flowchart of the optimization method is depicted in Figure 4.

## 5. Simulation results

### 5.1. Main parameters

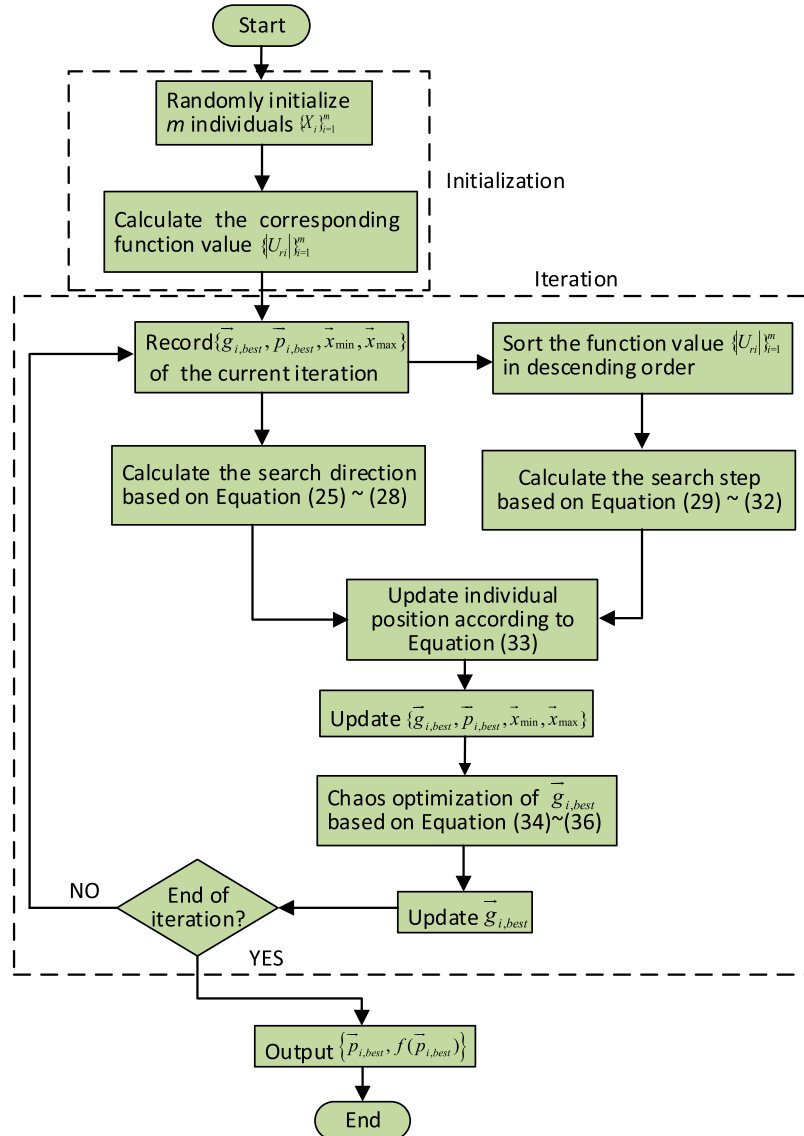
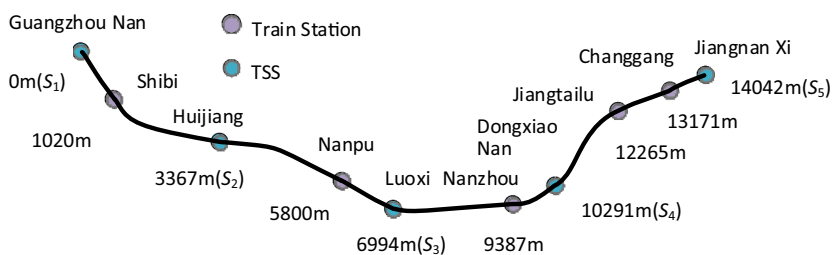
In this paper, simulations are carried out in Guangzhou Metro Line 2. The distribution of stations in the line is depicted in Figure 5. There are 10 train stations and  $S_1 \sim S_5$  are TSSs. The simulations are carried out during the period of 1100 s to 1280 s. The maximum rail potential is optimized based on the parameters of Guangzhou Metro Line 2 which are shown as follows:  $U_0 = 1593$  V,  $R_{eq} = 16$  mΩ,  $U_z = 1800$  V,  $Z_{un} = Z_{dn} = 20$  mΩ/km,  $Z_r = 20$  mΩ/km,  $Z_s = 20$  mΩ/km,  $G_r = 15$  Ω·km,  $G_s = 3$  Ω·km,  $T_{\max} = 1230$  s. The Logistic parameter  $\mu$  is 3.99 in this paper. Figure 6 shows the train diagram. Under the complex working conditions of the system, the departure interval of the trains is 180 s, and the dwell time at each station is set to 30 s before optimization.

Simulation model of DC traction power system is built in Part 3 to calculate the rail potential. In order to verify the reliability of the simulation model, a diagram is employed for field tests on 16 August 2016. In the diagram, two trains accelerated simultaneously at 26 s, driving in opposite directions. One train departed from Dongxiao Nan to Nanzhou and the other train departed from Nanpu to Luoxi. The simulation has also been carried out with the same diagram. Under this condition, there is little power coincidence between the accelerating train and the regenerative braking train because of the same departure time. As shown in Figure 7, the variation trend of simulation results is almost the same as that of field tests in the model validation. Besides, the maximum rail potential is 42.9 V in field tests, which is larger than that of the simulation. With the operation of running rails in the line, the joint resistance of the running rails as well as the cables will increase. In addition, the cross-section area of the running rails will reduce to a certain extent. These factors will make the longitudinal resistance of the running rail increase, and ultimately lead to the increase of rail potential in the field test.

### 5.2. Dynamic reflux safety parameters before optimization

Figure 8 shows the rail potential in the whole line before the optimization. Rail potential in the line frequently rises abnormally. The maximum rail potential is 136.3 V which is far beyond the standard limit. Figure 8(b) demonstrates that the rail potential rises abnormally at both ends during period of 1100 s to 1280 s.

When the rail potential at OVPD is over the safety limit of 90 V, the OVPD will be closed to connect the running rails to the ground, thereby reducing the rail potential immediately. If all the 5

**Figure 4.** Flowchart of improved SOA.**Figure 5.** Positions of stations and TSSs.

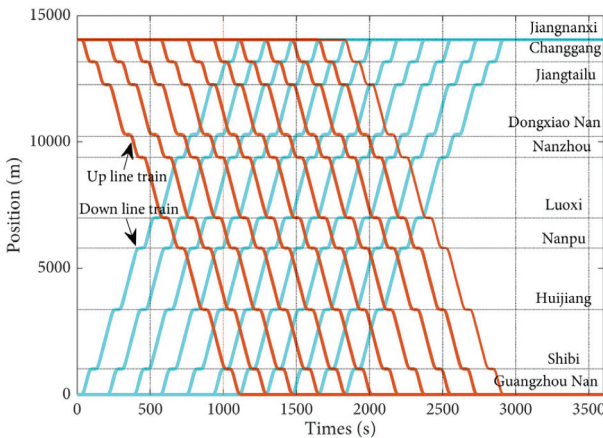


**Figure 6.** Train diagram before optimization.

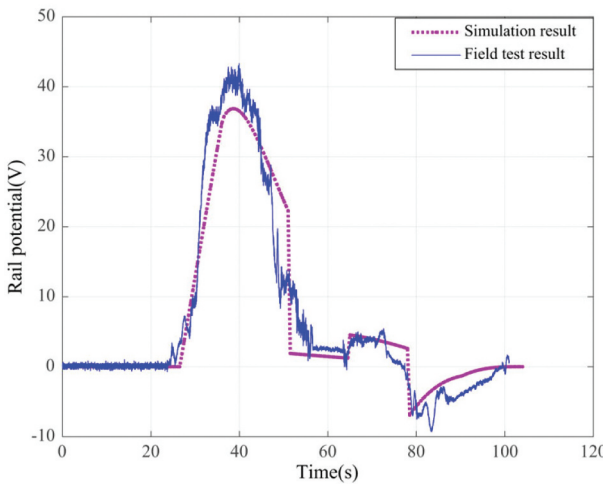


**Figure 7.** Model validation.

OVPDs at TSSs work normally, the distribution of reflux safety parameters is shown as Figure 9. In Figure 10(a), the red and blue areas demonstrate that the excessive rail potential still exist at different positions even if all the OVPDs work normally. The stray current distribution with all OVPDs working normally is depicted in Figure 10(b). During the same period, the stray current rises obviously and even reaches thousands of amperas. The stray current is almost the same in the same interval. Obviously, the power supply safety of the system cannot be guaranteed with OVPD action.

Before the optimization of the train diagram, the stray current of the system is depicted in Figure 9. The distribution of stray current in the entire line shows a trend of low at both ends of the line and high in the middle of the line. During the dynamic operation from 1100 s to 1280 s, the maximum stray current is 28.9 A, which appears at 7761 m and at 1264 s.

When the OVPD at TSS is triggered to be closed, a large amount of return current will flow into the earth through the closed OVPD, forming the leakage current. The distribution of leakage current with all the OVPDs working normally is shown in Figure 11, which indirectly proves the existence of excessive stray current under this situation. For the existence of

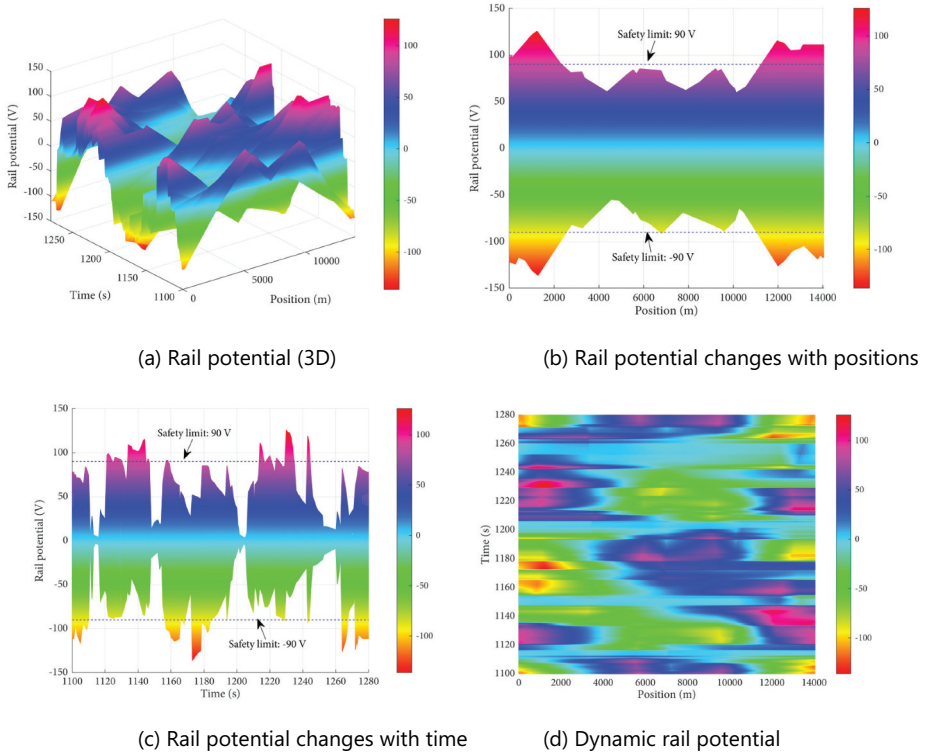


**Figure 8.** Dynamic distribution of rail potential before optimization.

massive rail potential, the OVPDs at  $S_1$  and  $S_2$  are triggered to connect the running rails to the ground at 1175 s and last for 10 s. The OVPDs at other TSSs are also triggered after 1 s and keep closed for 10 s. At 1177 s, the leakage current flowing from the OVPDs at  $S_1$  and  $S_2$  are 688.6 A and 353.9 A, respectively, and the leakage current flowing through the ground to  $S_3$ ,  $S_4$  and  $S_5$  are 625.3 A, 304 A and 113.2 A respectively, which significantly intensifies the stray current.

### 5.3. Rail potential optimization based on improved SOA

The improved SOA proposed in this paper is adopted to optimize the train diagram for safe operation of the system. The size of population  $m$  is 40. The number of iterations is 120. The number of decision variables  $N$  is 18 according to the actual line. The range of the dwell time is 20 s to 40 s.

As depicted in Figure 12, under the same initial conditions, the maximum rail potential is optimized by improved SOA, Genetic Algorithm (GA) and Particle Swarm Algorithm (PSO). Although GA has good global search capabilities, it can quickly search out all solutions in the solution space, the local search ability of GA is poor, which makes GA prone to premature phenomenon. Moreover, for the strong randomness in the parameter settings of GA and PSO, the convergence effect is often unstable. While the improved SOA algorithm proposed in this paper only uses function values to evaluate the pros and cons of individuals in the search process, and the function values are considered as a basis for updating the position of individuals, so that the initial solution is gradually optimized. The improved SOA algorithm proposed in this paper has good robustness and can effectively find the global optimal

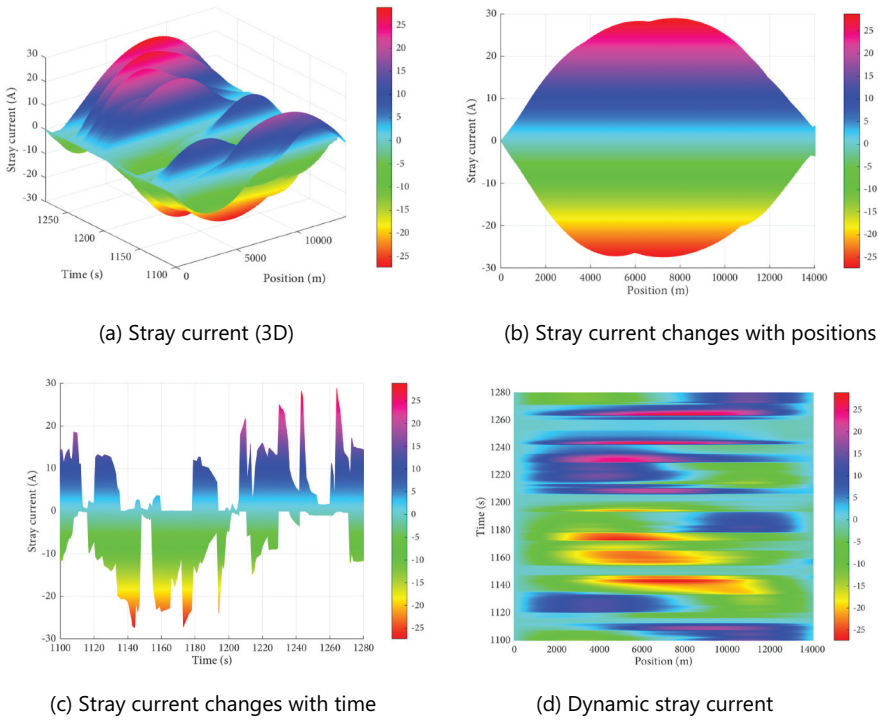


**Figure 9.** Dynamic distribution of stray current before optimization.

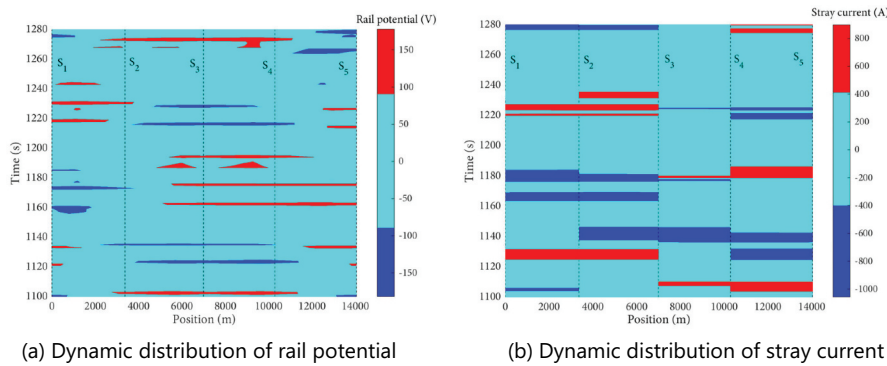


**Figure 10.** Distribution of reflux safety parameters with all the OVPDs working normally.

solution. The optimization result of the improved SOA algorithm is 60.7 V, which is much better than that of PSO (98.3 V) and GA (117.5 V). The convergence processes of the three algorithms are different. As depicted in Figure 12, GA and PSO show obvious premature phenomenon. Although the function values they currently searched are still large, even above the safety limit of 90 V, they start to converge completely at the 63th iteration and 73th iteration respectively. This phenomenon is due to that the two algorithms cannot get out of the local optimal situation under the complex running conditions of the system. But the improved SOA shows a fast and effective convergence process. In the first 25 iterations, SOA algorithm quickly and effectively utilizes the function values to evaluate individuals, which accurately determines the individuals' search steps and search directions. As a result, the

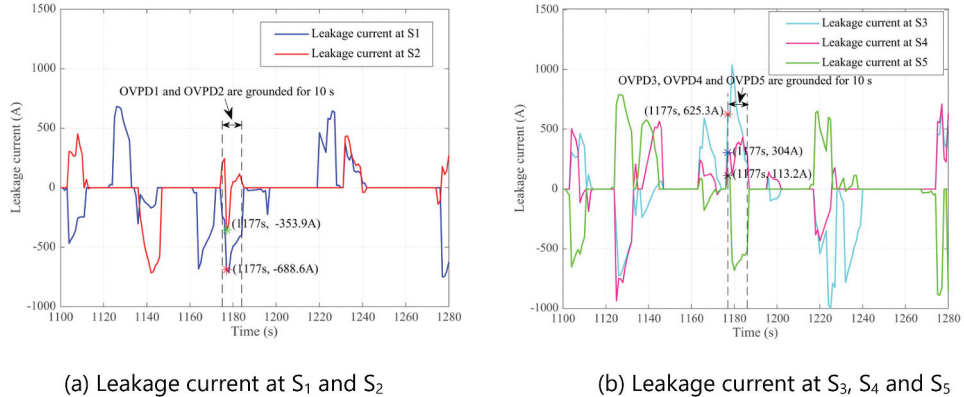


Figure 11. Distribution of leakage current.

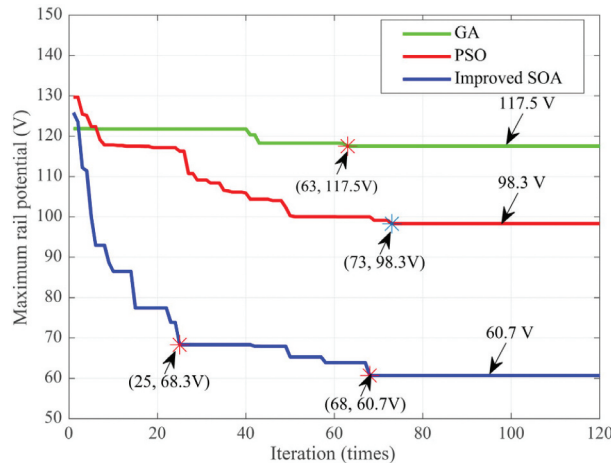
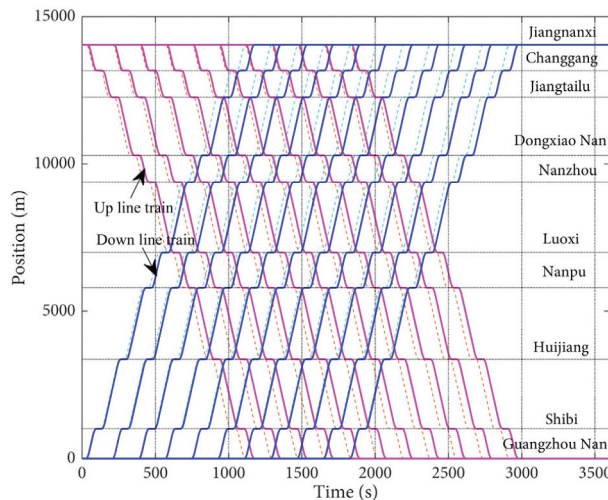


Figure 12. Convergence curves of maximum rail potential based on different algorithms.

current global optimal value quickly evolves from 125.8 V to 68.3 V at the 25th iteration. In the 26th to 68th iteration when the diversity of individuals is gradually decreasing, the algorithm can still converge relatively slowly because the chaotic optimization is performed and the secondary perturbation has happened to the current individuals, which increases the diversity of individuals and prevents algorithm from stagnating. Since the algorithm has maintained a high global search capability and maintain great diversity during the early and mid-to-late search process, the global optimal solution can be quickly found before about last 30 iterations. The corresponding dwell time of up line train and down line train obtained by improved SOA is expressed as  $X^* = [38 \text{ s}, 38 \text{ s}, 38 \text{ s}, 36 \text{ s}, 38 \text{ s}, 33 \text{ s}, 32 \text{ s}, 38 \text{ s}, 38 \text{ s}, 28 \text{ s}, 38 \text{ s}, 38 \text{ s}, 38 \text{ s}, 37 \text{ s}, 38 \text{ s}, 36 \text{ s}, 38 \text{ s}]$ .

The power coincidence degree of the accelerating trains and braking trains is controlled by adjusting the train diagram, thereby suppressing the maximum rail potential of the system. The comparison of train diagrams before and after optimization is shown in Figure 13. In Figure 13, the dashed and solid lines, respectively, represent the train diagrams before and after optimization. The total travel time is 1118 s and 1177 s before and after optimization respectively. According to Table 1, there is a minor adjustment range [-10 s, 10 s] at each station and the total adjustment values of both up line and down line train are all 59 s, with



**Figure 13.** Comparison of train diagrams before and after optimization.

**Table 1.** Comparison of dwell time before and after optimization.

Station Number	1	2	3	4	5	6	7	8	9	Total time
$t_{un}$ (s)	38	38	38	36	38	33	32	38	38	329
Adjustment value (s)	+8	+8	+8	+6	+8	+3	+2	+8	+8	+59
$t_{dn}$ (s)	28	38	38	38	38	37	38	36	38	329
Adjustment value (s)	-2	+8	+8	+8	+8	+7	+8	+6	+8	+59

a change of 5%. The total travelling time is slightly larger compared with that before optimization, while the reflux safety parameters will be significantly controlled.

When the optimization result  $X^*$  based on the improved SOA is used to manage the operation of trains, the rail potential after optimization is depicted in Figure 14. Compared with that before optimization, the maximum rail potential has been significantly reduced at each position. The maximum rail potential of the entire line is 60.7 V, which is 55.5% less than that before optimization. Figure 15 depicts the optimization result of stray current. The stray current also obviously decreases after optimization, which drops to 14.1 A, with a reduction of 51.2%. Therefore, the multitrain dwell time management scheme can effectively realize the control of the reflux safety parameters.

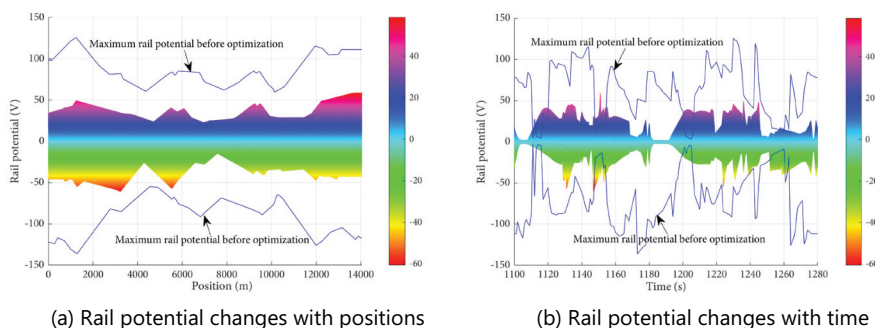


**Figure 14.** Dynamic distribution of rail potential after optimization.

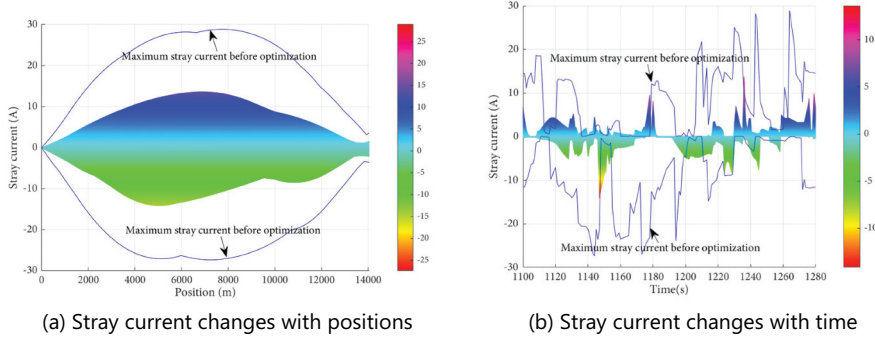


**Figure 15.** Dynamic distribution of stray current after optimization.

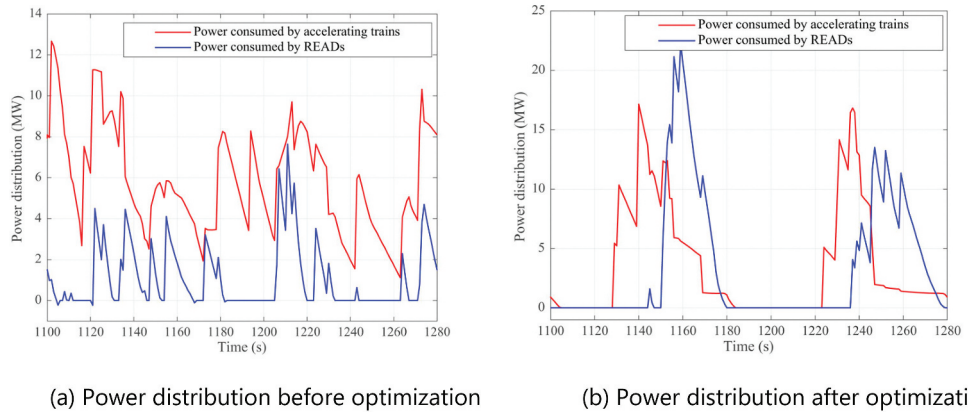


**Figure 16.** Comparison of regenerative braking power distribution before and after optimization.

The power coincidence between the accelerating trains and the regenerative braking trains affects the safe operation of the line. As depicted in Figure 16(a), before the optimization of the train diagram, the power coincidence between the accelerating trains and the regenerative braking trains is relatively high. At this time, the regenerative power transferring over zones is relatively large which is up to 290.4 kW·h. The rail potential frequently exceeds the safety limit, which is up to 136.3 V. As depicted in Figure 16(b), after the optimization of the train diagram, more regenerative energy is consumed by READs. The power coincidence between the accelerating trains and the regenerative braking trains during the dynamic operation is significantly dropped and the power transferring over zones is 179.1 kW·h during this period which is reduced by 38.3%. In addition, the corresponding maximum rail potential is also greatly reduced to 60.7 V which has reduced by 55.5%.

In order to analyse the variation in the rail potential distribution before and after optimization, the frequency of the rail potential on the whole line is counted in this paper, as shown in Figure 17. After the train diagram optimized by the improved SOA, the values of rail potential on the entire line are mostly limited between  $-30 \text{ V} \sim 30 \text{ V}$ , which are far below the safety limit of 90 V. While the probability of rail potential in the same range is much lower before optimization, which proves that the method proposed in this paper is effective in inhibiting rail potential. The optimized train diagram in this paper can make the system operate more safely.

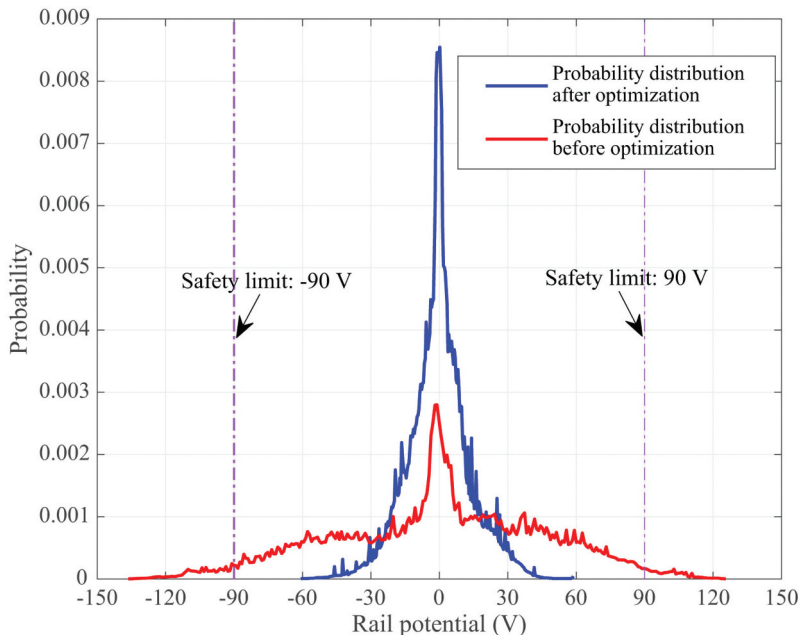


Figure 17. Comparison of the probability distribution of rail potential before and after optimization.

## 6. Conclusion

In this paper, the maximum rail potential is optimized by adjusting the train diagram of Guangzhou Metro Line 2 based on the improved SOA algorithm. The simulation model of DC traction power system and the calculation process of rail potential under the complex working conditions of the system is proposed. The rail potential is effectively suppressed by changing the power distribution of the system. Based on the parameters of Guangzhou Metro Line 2, the simulations are carried out. The maximum rail potential is 136.3 V which is far beyond the standard limit before optimization. The improved SOA algorithm is employed to optimize the rail potential of the system, compared with the simulation results of PSO and GA, the convergence effect is obviously better. After optimization with improved SOA, the maximum rail potential of the entire line has reduced to 60.7 V which is far below the safety limit. The power coincidence between the accelerating trains and the regenerative braking trains of the system is significantly dropped. Simulation results demonstrate that the improved SOA can greatly suppress the maximum rail potential which has been reduced by 55.5% after optimization. Therefore, the proposed method can ensure the safe operation of multitrain DC traction power system. The subway companies are trying and exploring the optimization of train diagrams to achieve energy saving and power supply safety of the system. With the rapid development of automatic train operation, the operability of the optimization of train diagrams will be further strengthened, which is of practical significance for the development of the future subway system.

## Disclosure statement

No potential conflict of interest was reported by the author(s).

## Funding

This work was supported in part by the National Natural Science Foundation of China under Grant 52007128, Grant 52075353 and Grant 51907137, in part by the Suzhou Prospective Research Program under Grant SYG201932, in part by the National Rail Transportation Electrification and Automation Engineering Technology Research Centre under Grant NEEC-2019-B07, in part by the China Postdoctoral Science Foundation 2020M681693; China Postdoctoral Science Foundation [2020M681693]; National Natural Science Foundation of China [51907137,52007128,52075353]; National Rail Transportation Electrification and Automation Engineering Technology Research Centre [NEEC-2019-B07]; Suzhou Prospective Research Program [SYG201932];

## References

- [1] Park J. Ground fault detection and location for ungrounded dc traction power systems. *IEEE Trans Veh Technol.* **2015**;64(12):5667–5676.
- [2] Charalambous C, Aylott P, Buxton D. Stray current calculation and monitoring in dc mass-transit systems: interpreting calculations for real-life conditions and determining appropriate safety margins. *IEEE Veh Technol Mag.* **2016**;11(2):24–31.
- [3] Gu J, Yang X, Zheng T. Influence factors analysis of rail potential in urban rail transit. *Microelectron Reliab.* **2018**;88:1300–1304.
- [4] Chen S, Hsu S, Tseng C, et al. Analysis of rail potential and stray current for Taipei metro. *IEEE Trans Veh Technol.* **2006**;55:67–75.
- [5] Paul D. Dc stray current in rail transit systems and cathodic protection. *IEEE Ind Appl Mag.* **2016**;22(1):8–13.
- [6] Ogunsola A, Sandrolini L, Mariscotti A. Evaluation of stray current from a dc-electrified railway with integrated electric-electromechanical modeling and traffic simulation. *IEEE Trans Ind Appl.* **2015**;51(6):5431–5441.
- [7] Railway Applications—Fixed installations—electrical safety, earthing and the return circuit—part 1: protective provisions against electric shock, standard 62128-1, Sep. **2013**.
- [8] Xu S, Li W, Wang Y. Effects of vehicle running mode on rail potential and stray current in dc Mass transit systems. *IEEE Trans Veh Technol.* **2013**;62(8):3569–3580.
- [9] Alamuti M, Zare A, Savaghebi M. Reversed diode earthing scheme in DC traction power system. International Universities Power Engineering Conf, Padova, Italy, January, **2008**; 1–5.
- [10] Tzeng Y, Lee C. Analysis of rail potential and stray currents in a direct-current transit system. *IEEE Trans Power Del.* **2010**;25(3):1516–1525.
- [11] Yang X, Li X, Gao Z, et al. A cooperative scheduling model for timetable optimization in subway systems. *IEEE Trans Intell Transp Syst.* **2013**;14(1):438–447.
- [12] Su S, Li X, Tang T, et al. A subway train timetable optimization approach based on energy-efficient operation strategy. *IEEE Trans Intell Transp Syst.* **2013**;14(2):883–893.
- [13] Pena M, Fernandez A, Cucala A, et al. Optimal underground timetable design based on power flow for maximizing the use of regenerative-braking energy. *Proc Inst Mech Eng F J Rail Rapid Transit.* **2012**;226(4):397–408.
- [14] Chen Y, Mao B, Bai Y, et al. Timetable synchronization of last trains for urban rail networks with maximum accessibility. *Transp Res Part C Emerging Technol.* **2019**;99:110–129.
- [15] Zhu Y, Mao B, Bai Y, et al. A bi-level model for single-line rail timetable design with consideration of demand and capacity. *Transp Res Part C Emerging Technol.* **2017**;85:211–233.
- [16] Li Q, Wang T, Li S, et al. Online extremum seeking-based optimized energy management strategy for hybrid electric tram considering fuel cell degradation. *Appl Energy.* **2021**;285:116505–116516.
- [17] Li Q, Yin L, Yang H, et al. Multi-objective optimization and data-driven constraint adaptive predictive control for efficient and stable operation of PEMFC system. *IEEE Trans Ind Electron.* **2020**;1. Early Access. doi:[10.1109/TIE.2020.3040662](https://doi.org/10.1109/TIE.2020.3040662)
- [18] Xu X, Zhao J, Xu Z, et al. Stochastic optimal TCSC placement in power system considering high wind power penetration. *IET Gener Transm Distrib.* **2018**;12(12):3052–3060.
- [19] Malladi K, Sowlati T. Biomass logistics: a review of important features, optimization modeling and the new trends. *Renew Sust Energ Rev.* **2018**;94:587–599.
- [20] Hachem H, Gheith R, Aloui F, et al. Technological challenges and optimization efforts of the Stirling machine: a review. *Energy Convers Manag.* **2018**;171:1365–1387.
- [21] Liu W, Luo N, Pan G, et al. Chaos particle swarm optimization algorithm for optimization problems. *Int J Pattern Recognit Artif Intell.* **2018**;32(11):18.
- [22] Du G, Zhang D, Li G, et al. Evaluation of rail potential based on power distribution in DC traction power systems. *Energies.* **2016**;9(9):729.

- [23] Lin F, Lin S, Yang Z. Multi-train energy saving for maximum usage of regenerative energy by dwell time optimization in urban rail transit using genetic algorithm. *Energies.* 2016;9(3): 208.
- [24] Du G, Wan J, Zhu Z, et al. Effect of crossing power restraint on reflux safety parameters in multitrain subway systems. *IEEE Trans Transport Electrific.* 2019;5(2):490–501.